

Light-Alignment Controllable Beam Splitter and Vectorial Displacement Sensor in the Stopped-Light Regime of Plasmonic Metasurfaces

Maria I. Benetou* and Kosmas L. Tsakmakidis



Cite This: *ACS Photonics* 2021, 8, 296–306



Read Online

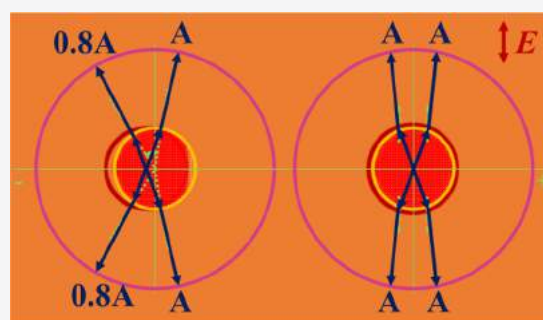
ACCESS |

Metrics & More

Article Recommendations

ABSTRACT: We report the experimental realization of periodically perforated plasmonic metasurfaces capable of integrating several key functionalities, such as light-to-surface plasmon coupling, controllable beam-splitting, wavelength filtering and routing, high resolution differential wavelength measurement, and vectorial displacement sensing. The plasmonic metasurfaces operate at telecom wavelengths, at the vicinity of the eigenmode crossing points where zero group velocity is experienced, and their functionality parameters, such as sensitivity to misalignment, prong angular separation, power ratio, polarization, and bandwidth, can be adjusted by designing the boundary shape and by conveniently manipulating their alignment with the illuminating light beam. In the same context, a circular plasmonic metasurface could also serve as a *vectorial* displacement sensor capable of monitoring simultaneously the magnitude and direction of the displacement between its center and that of the illuminating beam. The compact, easily controllable, and all-in-one nature of our devices can enable on-chip integrated circuits with adaptable functionality for applications in sensing and optical signal processing.

KEYWORDS: *metasurfaces, slow light, metamaterials, wavelength routing, optical communications, plasmonic crystals, surface dispersion engineering*



The integration of photonic functionalities, along with the reduction in size of integrated photonic systems for on-chip information processing and sensing, are essential elements for ongoing advancements in diagnostics medicine, phototherapy, space missions, manufacturing quality control, optical computing, and short-range communication systems. Over the past two decades, plasmonics has emerged as a potential road to compact and fast devices.^{1–12} Plasmonics is a flourishing field of science exploiting surface plasmons, the collective oscillations of free electrons on a metal-dielectric interface, to route and manipulate light at nanometer length scales.^{13–15} Plasmonic components feature ultracompact geometries, and can be controlled more flexibly, and often more energy-efficiently too, compared to standard dielectric components, owing to the enabled strong field confinement and enhancement.^{16,17} Combining the size of nanoelectronics¹⁸ with the speed of dielectric photonics, they enable devices that can naturally interact with both technologies.^{6,14} Recently researchers have also started investigating plasmonics in the quantum regime.^{19,20} Plasmonic nanostructures²¹ and metasurfaces²² can be designed to perform mathematical operations on light signals, forming among others a basis for compact optical and quantum computing.

Beam splitters and wavelength filters are some of the most used elements in photonic integrated circuits. Very recently, it has been proposed²³ that the decomposition and implementation of any general linear transformation can be achieved using lossy plasmonic beam splitters. The loss of the inherently lossy plasmonic beam splitters can be viewed as a degree of freedom, as it relaxes the requirement for a $\pm 90^\circ$ phase difference between the transmission and reflection factors existing in the nonlossy, unitary beam splitters.^{23–27} Plasmonic beam splitters have also recently been used to realize a quantum random number generator²⁸ and to conduct the plasmonic version^{24,29} of the Hong-Ou-Mandel (HOM) experiment,³⁰ at which plasmon coalescence and anticoalescence were observed depending on the transmission and reflection factors of a plasmonic beam splitter.²⁴ The plasmonic test platform in ref 24 had a $40 \mu\text{m} \times 40 \mu\text{m}$ footprint, and consisted of photon-

Received: September 30, 2020

Published: December 29, 2020



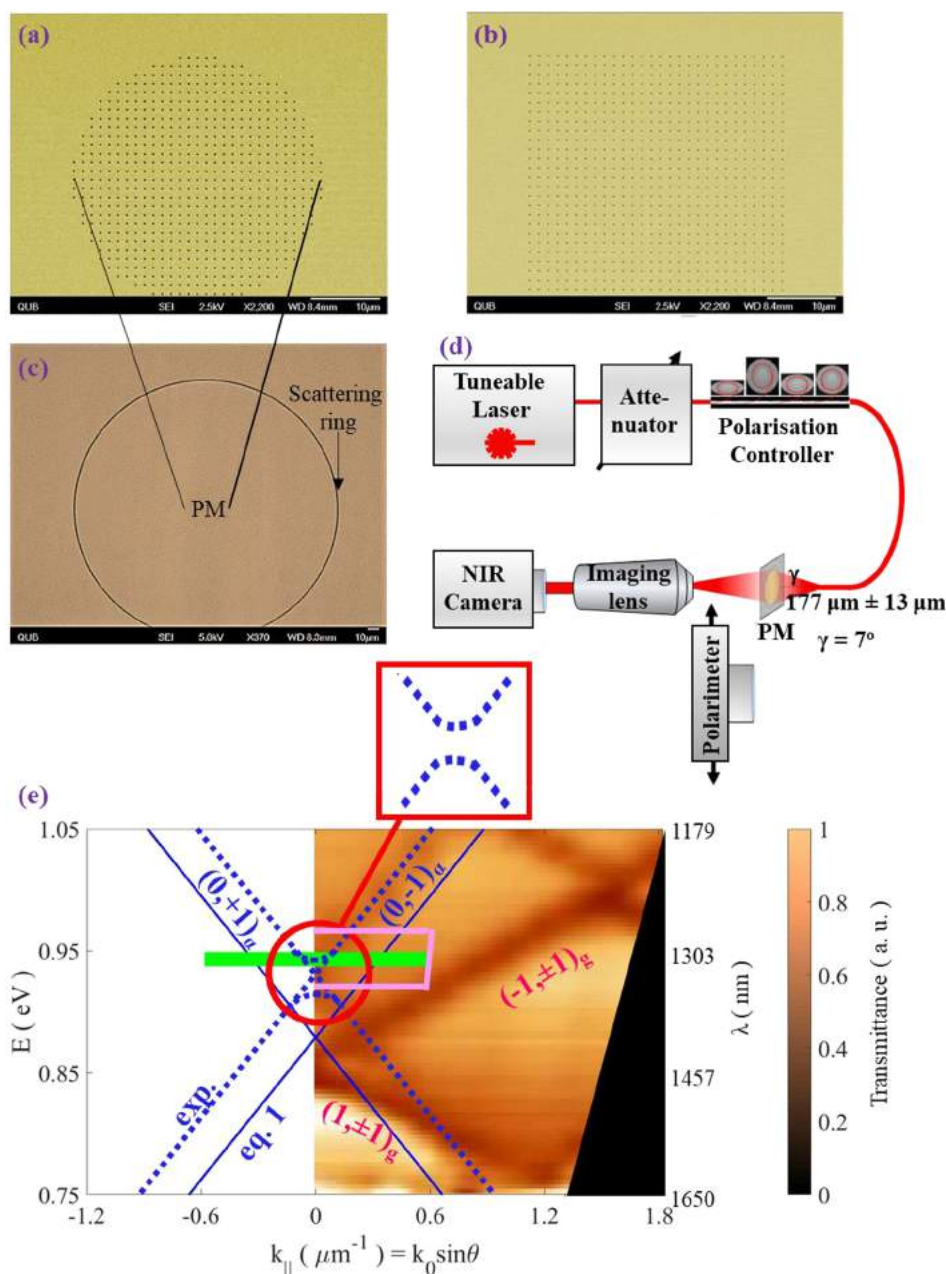


Figure 1. (a–c) SEM images of (a) the circular and (b) the square boundary plasmonic metasurfaces and (c) the circular boundary plasmonic metasurface and the surrounding scattering ring. (d) Experimental arrangement for imaging the far-field light intensity distribution corresponding to the SPP intensity distribution. (e) Measured plasmonic metasurface transmission dispersion 2D map (the experimental air-Au eigenmode positions are marked with blue dotted lines) and estimated air-Au eigenmode positions using eq 1 (solid blue lines). The labels corresponding to the air-Au are denoted by “a”. The experimental glass-Au eigenmodes are marked with pink labels containing the subscript “g”. The spectral area where the experimental air-Au eigenmodes flatten to avoid crossing is marked with a red circle and enlarged at the inset. The spectral areas excited when the sample is illuminated with the experimental arrangement shown in (d) with vertically polarized monochromatic light ($\lambda = 1313/1319$ nm) (green line) or with wavelength ranging from 1280 to 1345 nm (pink box) are shown. The black (triangular) area is a spectral area which is not covered with experimental data.

to-SPP converters, an SPP beam splitter whose reflection and transmission factors were a function of its geometrical parameters (i.e., stayed fixed after fabrication), and SPP-to-photon converters.

In this work, we present judiciously designed multifunctional plasmonic metasurfaces (PMs) consisting of subwavelength holes periodically perforated on a subwavelength-thickness metal film attached on a glass substrate. Our structures integrate photon-to-SPP conversion with SPP beam splitting, wavelength filtering and routing, and can perform high

resolution differential wavelength measurement and vectorial displacement sensing (i.e., they can measure the magnitude and direction of the displacement between the structure and the incident beam). Differently from beam splitter structures based on two Bragg gratings^{31,32} with different bandgaps, positioned in opposite directions, which split different wavelengths in opposite directions by operating as rejection band filters^{33,34} for the bandgap wavelengths, our metasurface can split a *monochromatic* beam in multiple prongs. In beam-splitting applications, characteristics such as the spatial

configuration and the polarization of the output beams are of prime interest. In the case of the most commonly used plasmonic beam splitters^{23,24,28,29} which split a monochromatic plasmonic beam in two prongs based on the partial reflection of a propagating plasmonic beam, the two output beams propagate orthogonally to each other and, following the plasmonic TM nature, are orthogonally polarized. In contrast, the four outputs of the plasmonic beam splitters presented in this work propagate in either (anti)parallel directions or in small angles between them, with similar polarizations to each other and retaining to a relatively high degree the polarization of the incident light beam.

The principle on which the beam-splitting devices presented in this work function is based on the well-known eigenmode flattening at the edge of a bandgap^{32,34,35} and the ensuing zero group velocity points.^{32,34,36–39} When an extended spectral area that includes the flat-eigenmode area is excited, each of the excited and propagating (at the + and – directions) beams is forced to split into two prongs resulting in a 1×4 beam splitting. The functionality parameters of the structures, namely the sensitivity to misalignment, the output prong angular separation, power ratio, propagation direction, polarization, and bandwidth are here determined by the boundary shape of the structures and can be further controlled by manipulating their alignment with the illuminating beam.

Alongside with the beam-splitting functionality, we show that the circular structures we designed can also serve as high-resolution vectorial displacement sensors, capable of monitoring simultaneously the magnitude and direction of the displacement between the plasmonic metasurface structure and the illuminating beam centers. This vector-displacement information, along with the microscale size, and the overall reduced complexity, are highly sought-after characteristics for practical applications in the fields of mechanical engineering, space and military missions, robotic arms, and phototherapy.^{40–43} Although our structures have a $40 \mu\text{m} \times 40 \mu\text{m}$ footprint, same with that of the structure presented in ref 24, their size can be scaled down to $28 \mu\text{m} \times 28 \mu\text{m}$ (~ 441 holes) without changing their functionality.⁴⁴ Another advantage of the herein-presented plasmonic devices is that while a part ($\sim 8\%$)^{12,38} of the excited SPPs launch on the surrounding smooth metal film, the majority of them couple back into photons enhancing the transmission of the illuminating beam through the nanostructured area;^{10,15} the transmission of the illuminating beam through the nanostructured area is $\sim 25\%$, while the area of the plasmonic metasurface covered with holes is only 3%, and thus allows for nondestructive sensing or sampling, and parallel processing of the beam.

In addition, the output prong SPP beams demonstrate an angular wavelength dispersion; i.e., the output prong resonance wavelength can experience a red-shift or a blue-shift depending on its propagation direction. If the output prong SPP beams were to couple to waveguides, the resonance coupling wavelength could be fine-tuned by judiciously selecting the waveguide angular position around the plasmonic metasurface. The inherent SPP angular wavelength dispersion, enhanced by the interferences happening in the Fabry–Perot cavity formed between the substrate facets, enable the plasmonic metasurfaces to operate as high-resolution differential wavemeters, capable of detecting small differences in wavelengths by comparing the output prong SPP power at appropriately selected angular positions. The herein presented multifunc-

tional structure could become a vital element in adaptable, integrated photonic circuits for key applications in on-chip signal processing and sensing.

SAMPLES AND EXPERIMENTAL ARRANGEMENT

The plasmonic metasurfaces (PMs) used in the experiments were fabricated by focused ion beam (FIB) milling of a magnetron-sputtered 50 nm thick gold (Au) film attached on a 700 μm glass substrate. They consisted of 300 nm diameter circular holes, periodically perforated in a 1400 nm period square lattice, and they had either circular (40 μm diameter) or square (40 μm width) boundaries. Scanning electron microscopy (SEM) images of the samples are shown in Figure 1(a,b). The PM structures were surrounded by a 240 μm internal diameter, 1.5 μm width circular slit, as shown in Figure 1c, which allowed the SPP signal launching from the PMs onto the surrounding smooth metal film to be detected in the far-field, after scattering into photons.

The PM transmission dispersion, shown in Figure 1e, was investigated by measuring the zero-order far-field transmission spectra of the structures for different angles of incidence θ , under illumination with y-polarized light, as described in the literature.^{12,45} For the PM size used in this work, the far-field transmission dispersion is independent of the PM boundary shape and is essentially governed by the lattice parameters.³⁸ A periodically perforated plasmonic metasurface with a square lattice supports several SPP Bloch modes that are the eigenmodes of the structure,⁴⁶ and can be theoretically approximated using a perturbative approach, valid in the limit of infinitely small holes and away from the areas where the eigenmodes tend to cross,^{45,47} according to which the dispersion relation of the SPP Bloch modes can be written as the folding of the dispersion relation of the flat interface SPP (eq 1):

$$k_{\text{BSPP}} = k_{\text{SPP}} + \frac{2\pi}{D}(p\vec{u}_x + q\vec{u}_y) \quad (1)$$

where k_{BSPP} and $k_{\text{SPP}} \left(= \frac{2\pi}{\lambda} \sqrt{\frac{\epsilon_m \epsilon_d}{\epsilon_m + \epsilon_d}} \right)$ are the wavevectors of

the SPP Bloch modes on the periodically perforated plasmonic metasurface and the SPPs on a smooth surface, respectively, D is the lattice period, u_x and u_y are the unit vectors of the reciprocal lattice, p and q are integers related to the several diffraction modes, λ is the illuminating light wavelength, and ϵ_m , ϵ_d are the dielectric constant of metal and dielectric, respectively. This first approximation ignores⁴⁵ the effect of the hole geometric properties, namely shape and size, at the dispersion of the excited and propagating SPPs as well as their coupling which is particularly strong at the centers of the Brillouin zones—where the Bloch modes tend to cross. These eigenmodes can be identified in the PM transmission dispersion (Figure 1e) since they are responsible for the transmission enhancement.^{45,48,49} The blue solid lines show the analytically approximated eigenmodes for the air-Au interface, denoted with the subscript “a”, as estimated using eq 1. The corresponding experimental ones have been marked with blue dotted lines. Although eq 1 is only a first-order approximation, the analytically approximated eigenmodes are in relatively good agreement with the experimental ones at the areas away from the Brillouin zone center, where the eigenmodes tend to cross, except a small (~ 65 nm) spectral shift toward the larger wavelengths. The experimental

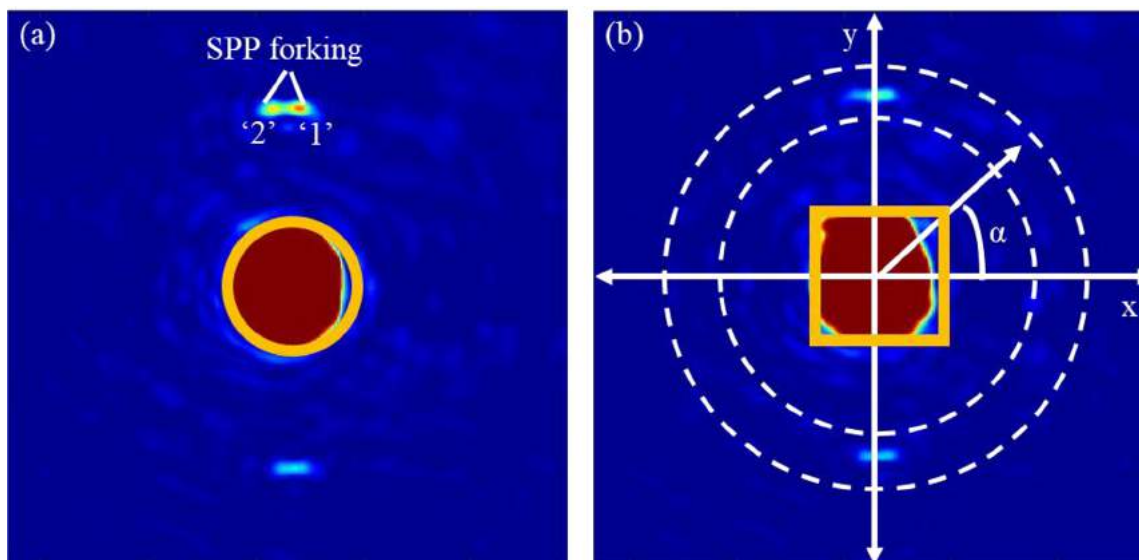


Figure 2. Far-field images of the SPP intensity on and around the (a) circular and (b) square plasmonic metasurfaces when off-centered illuminated with a monochromatic ($\lambda = 1313 \text{ nm}/1319 \text{ nm}$), vertically polarized laser beam out of a single mode fiber (N.A.: 0.13). The PM structures have been marked with a gold outline.

eigenmodes excited at the glass-Au interface are marked with pink labels containing the subscript “g”.

At the points where the eigenmodes tend to cross, SPP bandgaps, i.e., dark spectral areas at which the SPP wave excitation is forbidden, are formed and the SPP eigenmodes flatten to avoid crossing.^{35,50} Such a bandgap can be observed at the Brillouin zone center, where the $(0, +1)_a$ and $(0, -1)_a$ eigenmodes tend to cross and has been marked with a red circle. The spectral area is shown enlarged at the inset displaying the flattening of the experimental eigenmode curves. The SPP bandgaps are caused by the constructive interference of two counterpropagating SPP waves with the same frequency, arising from scattering at consecutive Bragg planes.^{35,45} This SPP modes coupling leads to a pronounced bending of the SPP dispersion,³⁵ giving the SPP eigenmode a standing wave character.^{36,37} Since the SPP coupling is ignored at the theoretical calculations using eq 1,⁴⁵ the SPP bandgaps and eigenmode bending is only observed in the experimental eigenmodes and not at the approximated theoretical ones. When the spectral area adjacent to SPP bandgap (marked with a green line) is excited with a monochromatic, divergent or convergent (i.e., consisted of a range of wavevectors) beam, the group velocity $v_g \left(= \frac{d\omega}{dk} \right)$ of the wavevectors corresponding to the flat eigenmode region (Brillouin zone center) tends to zero, and thus the SPP waves cannot propagate in this direction.

As a result, each of the SPP beams, consisting of the $(0, +1)_a$ and the $(0, -1)_a$ eigenmodes and propagating at the $+y$ and $-y$ directions, are forced to split into two prongs, corresponding to the two eigenmodes. This effect has been mentioned before in the bibliography as “SPP forking”,^{37,38} and it is the basis of the beam splitting functionality of the plasmonic metasurface presented in this work. Although the incurrence of the SPP beam splitting is governed by the lattice parameters, the structure functionality parameters, namely alignment sensitivity, and prong angular separation, power ratio tunability, propagation direction, polarization, and bandwidth depend on the PM boundary shape. This dependence has been

experimentally investigated in this work by characterizing and comparing the functionality parameters of the two PM structures shown in Figure 1a,b, which have the same lattice parameters but different boundary shapes, viz., circular and square.

The optical signal intensity distribution on the PM structures and the surrounding scattering ring, corresponding to the SPP signal intensity distribution, was captured using the experimental arrangement shown in Figure 1d. The PM structures were illuminated with a vertically polarized laser beam through a single mode fiber coupled to a polarization controller and a tunable infrared laser. The PM structures were positioned $177 \mu\text{m} \pm 13 \mu\text{m}$ from the fiber end; this fiber-sample separation was selected to illuminate the PM but not the surrounding scattering ring. The fiber numerical aperture was 0.13, offering a 7° divergent illumination. The illuminating light polarization was controlled by the polarization controller. The transmitted light was collected by an antireflection coated imaging lens ($\times 10$, NA:0.17) and detected by a high dynamic range (1800:1), near-infrared, InGaAs, charged-coupled (CCD) camera.

RESULTS AND DISCUSSION

Figure 2(a,b) shows the far-field SPP intensity distributions on and around the circular and square PMs, when these were illuminated off-center, viz., with a small horizontal displacement between the beam and PM centers, with vertically polarized monochromatic ($\lambda = 1313 \text{ nm}/1319 \text{ nm}$) light; the excited spectral area is denoted with a green line in Figure 1e. The central area is the image of the PM itself and it is saturated due to the high ($\sim 25\%$ of the illuminating beam) direct transmission through the nanostructured area.^{10,15} Because we detect the propagation on the smooth film SPP waves through far-field imaging, after being scattered onto the defect ring ($\sim 10\%$ efficiency), the coupling efficiency between the illuminating beam and the light detected on the camera at the prong positions is $\sim 0.2\%$. As expected from the transmission dispersion of the PMs (Figure 1e), the excited eigenmodes are the $(0, \pm 1)_a$ eigenmodes, excited at the air-Au

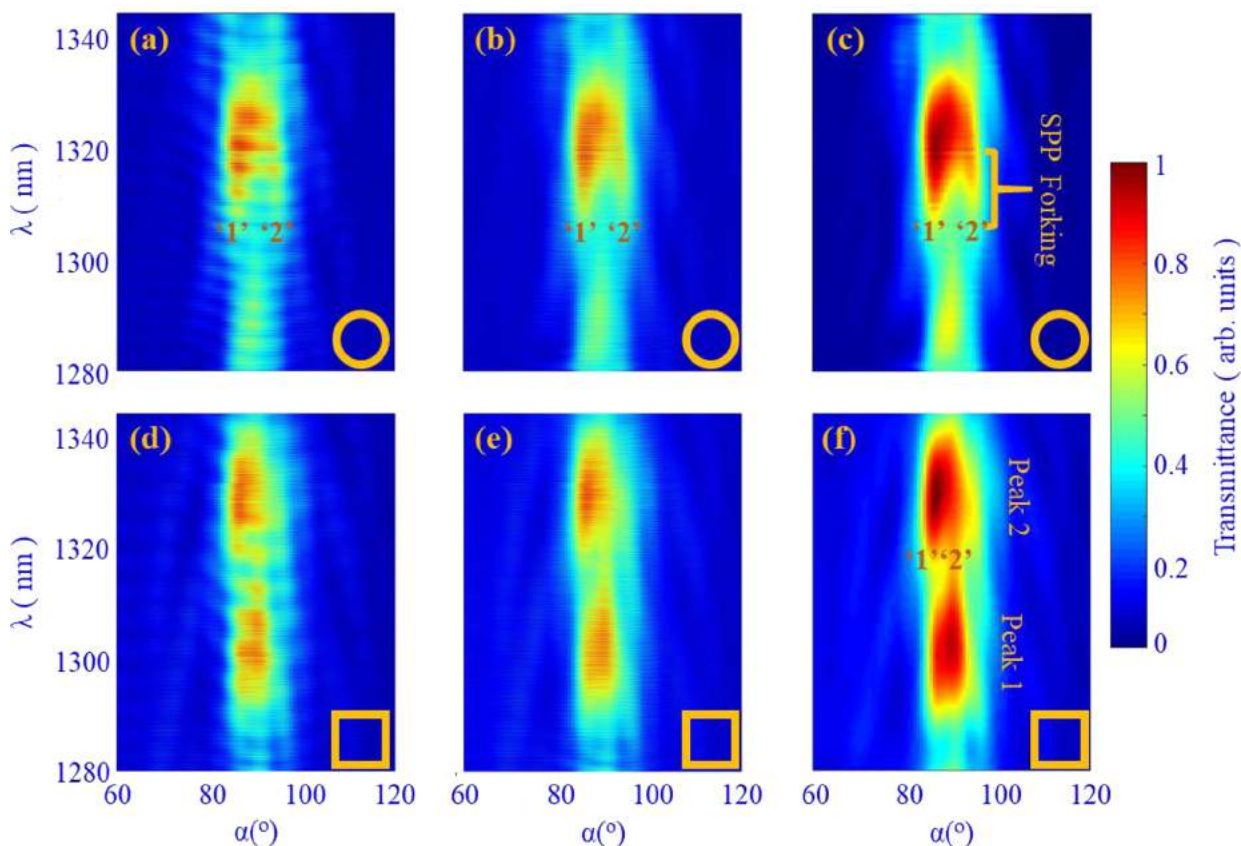


Figure 3. Normalized angular distribution of the SPP signal transmittance spectra at the upper half hemisphere around the circular and square boundary plasmonic metasurfaces (a,d) as measured and after mathematically filtering out (b,e) only the f-s cavity, (c,f) both the f-s and the substrate cavities. The inset at each figure shows the boundary shape of the plasmonic metasurface. The two SPP prongs are marked as “1” and “2”.

interface. The light observed around the angular positions $\alpha = 90^\circ$ and $\alpha = 270^\circ$ of the scattering ring corresponds to these eigenmodes.

As it is easily observed in Figure 2a, the surface plasmon polaritons do not propagate at the direction $\alpha = 90^\circ$, due to the zero group velocity experienced in this direction, and thus the beam propagating at the upper hemisphere splits into two prongs, marked as “1” and “2”, which are detected at the angular positions $\alpha = 86^\circ$ and $\alpha = 94^\circ$. Because of a small tilt of the normal PM with respect to the z -axis of the illuminating beam, the same splitting is not observed in the lower hemisphere.³⁸ For an ideal alignment between the normal to the PM and the beam z -axis, since the PM structure and the illumination are symmetrical with respect to the x -axis, the same splitting would be observed at the lower hemisphere, too, at around $\alpha = 270^\circ$, rendering an 1×4 beam-splitting functionality. The SPP prongs propagate individually and, after refracting at the PM boundary, launch on the surrounding smooth film. For a given wavelength value, the angle of incidence and thus the angle of refraction depends on the boundary curvature at the point that each of the prongs refracts and launches on the surrounding smooth metal film. The angular separation of the prongs can be controlled by designing the PM boundary.

The plasmonic metasurface structures presented in this work operate also as bandpass wavelength filters and routers. To quantitatively investigate the wavelength dependent SPP signal transmittance angular distribution, the illuminating wavelength was varied in the wavelength range 1280 to 1345 nm with a

0.005 nm resolution, the corresponding spectral area is marked with a pink box in Figure 1e, and the far-field SPP intensity distribution was imaged on the infrared camera for each value of the illuminating wavelength. Since the SPP excitation is polarization dependent,¹⁰ the illuminating light polarization was checked regularly, every 1 nm, and, if needed, it was readjusted to stay linear-vertical during the wavelength characterization of the samples. The captured images were first transformed into polar coordinates and then the optical intensity was integrated over an annular aperture that encompasses the scattering ring, as shown in Figure 2b, and over angular sections of 0.7° , corresponding to the camera pixels. The SPP signal transmittance for an illuminating wavelength λ was calculated as the ratio of the power at the angular position α when the sample is illuminated with the wavelength λ over the detected power in the absence of the sample for the same illuminating wavelength. Figure 3a,d shows the angular SPP transmittance in the upper hemisphere of the scattering ring surrounding the two structures, circular and square, as a function of the illuminating wavelength λ and the angle α , as defined in Figure 2b. The SPP beam splits into two prongs, marked “1” and “2”, and, as expected from the PM transmission dispersion spectrum (Figure 1e), prong “1” experiences positive angular wavelength dispersion ($\frac{d\lambda}{d\alpha} > 0$), i.e., the longer wavelength is detected in a bigger angle α , while prong “2” experiences negative wavelength dispersion, angular wavelength dispersion ($\frac{d\lambda}{d\alpha} < 0$), i.e., the shorter wavelength is detected in a smaller angle α . It is also clear that the prong

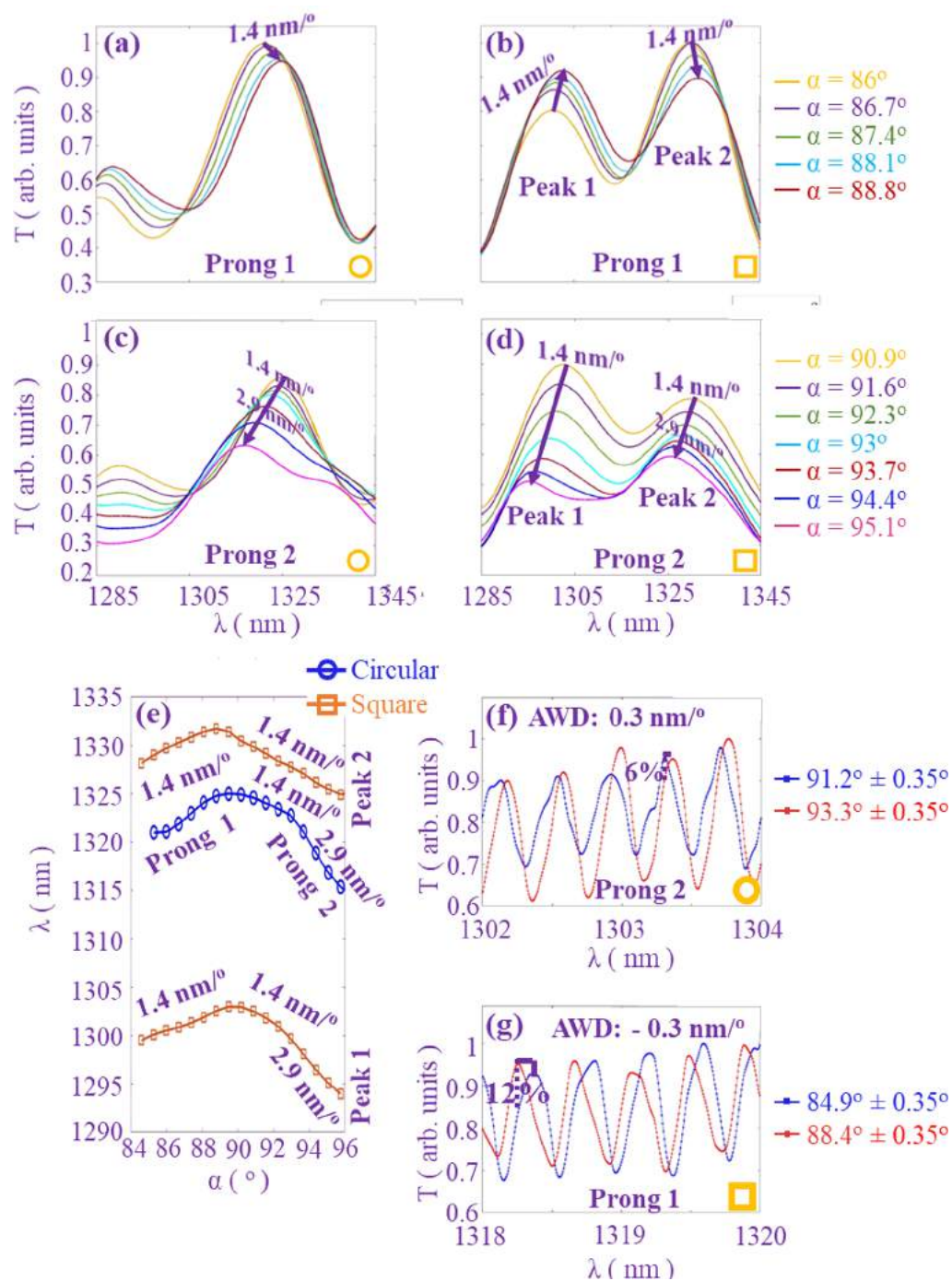


Figure 4. SPP signal transmission spectra at several angular positions α corresponding to (a,b,g) prong “1” and (c,d,f) prong “2”, after eliminating (a–d) both the f-s and substrate cavities, (f–g) only the f-s cavity. The PM boundary shape is shown at the inset of each figure. (e) Resonance wavelength of the spectra shown in (a–d) as a function of the angular position α .

angular separation is larger in the case of the circular structure, compared to that of the square structure. The observed small, 6 nm, spectral shift of the square structure transmittance spectrum toward longer wavelengths is due to a small tilt between the beam z -axis and the normal to the PMs, and has been taken into account when the two structures are compared for a given wavelength value, viz., in Figure 2 and Figure 5.

In addition to the inherent eigenmode angular wavelength dispersion, the effect of three Fabry–Perot cavities is prominent. The first cavity (f-s cavity, effective length: 177 μm), formed between the sample and the illuminating fiber, is

related to the experimental arrangement and can be easily eliminated with the use of an antireflection-coated patchcord.¹⁰ The second cavity (substrate cavity, effective length: 1050 nm) is formed between the two facets of the glass substrate and, if required, can be eliminated by using an antireflection coated or wedged substrate. The third cavity (PM cavity, effective length: 26 μm) is produced by the reflections between the SPP eigenmodes origin, i.e., the illumination spot center, and the PM boundary. Since the reflection of the SPP beams is stronger when the PM boundary is perpendicular to their propagation direction, the effect of the PM cavity is more

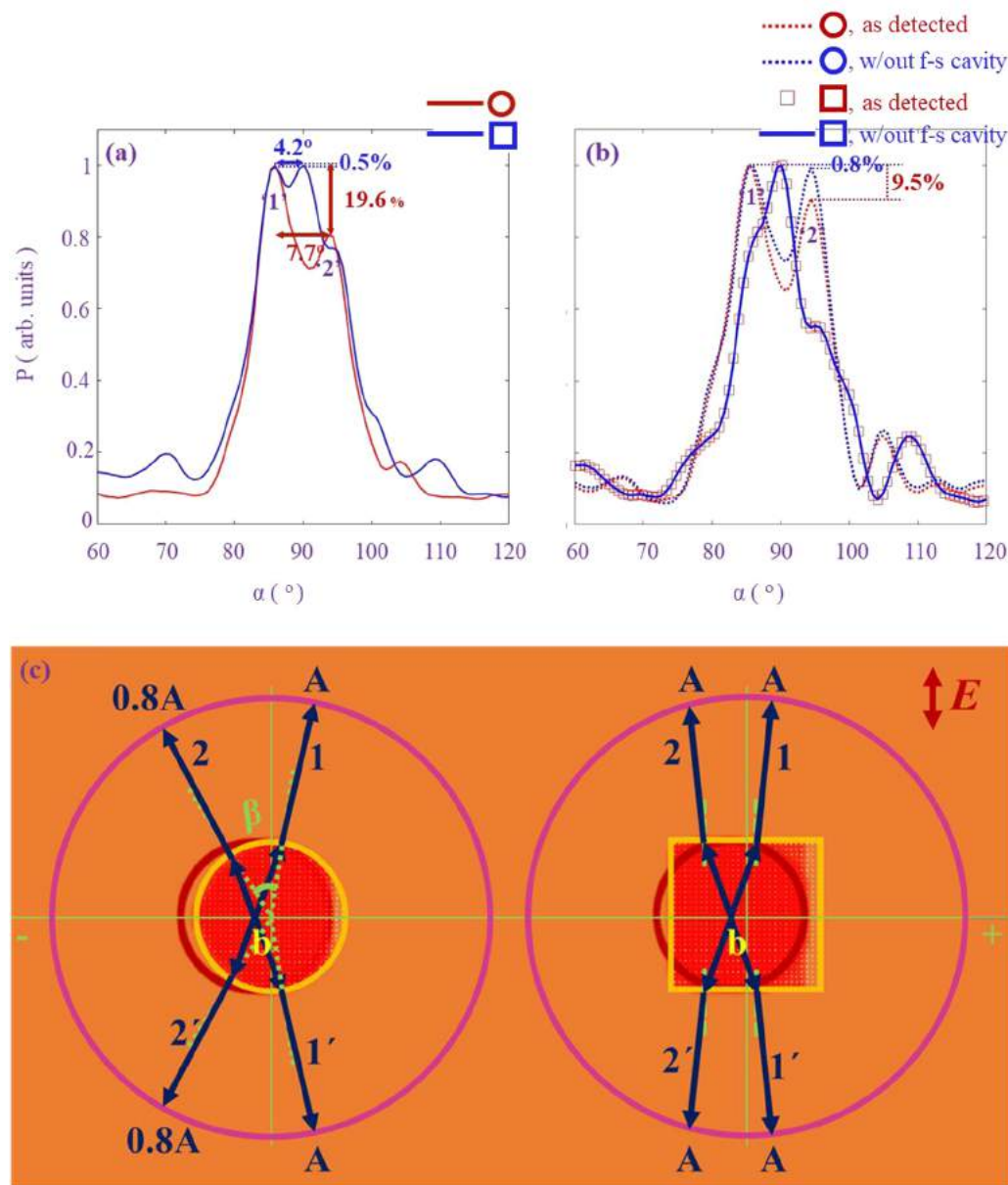


Figure 5. (a,b) SPP power angular profile at the upper hemisphere of the surrounding ring around the circular and square PMs when illuminated with $\lambda = 1313$ nm/1319 nm (a) after eliminating both the f-s and substrate cavities (b) as detected, and after eliminating the f-s cavity. (c) Schematic representation of the off-centered illumination of the plasmonic metasurfaces and the propagation of the four prongs (1, 2, 1', 2') on the nanostructured area and the surrounding smooth film until they impinge on the scattering ring, when there is no tilt between the out-of-plane z-axis beam and the normal to metasurface. The primed prongs (1', 2') have the same power as the corresponding nonprimed ones (1, 2) due to the symmetry of the structure and illumination in respect to the horizontal axis. The illuminated beams are marked with red circles, the PMs with gold outlines surrounding subwavelength holes assemblies, and the scattering rings with pink circles surrounding the PMs.

prominent for the case of the square structure than the circular one. To separate the effects of the Fabry–Perot cavities from the eigenmode angular wavelength dispersion, the wavelength dependent angular transmission spectra of the two structures have been plotted after mathematically filtering out only the f-s cavity (Figure 3b,e) and both the f-s and the substrate cavities (Figure 3c,f). By taking vertical cross sections of Figure 3(c,f) the transmission spectra, at several angular positions α around the two structures corresponding to the two prongs, after eliminating the f-s and substrate cavities, have been plotted in Figure 4(a–d).

Because of the PM cavity, the SPP transmission spectra around the square structure, at the wavelength range 1285 to

1345 nm, consists of two resonance wavelength peaks, marked as peak 1 and peak 2, and the 3-dB bandwidth, i.e., the wavelength range over which the detected SPP power is more than 50% of the maximum detected SPP power, is almost double (53 nm) compared to that one of the circular structure (35 nm) whose transmission spectra consist of only one resonance wavelength peak. The 3-dB bandwidth can be adjusted by manipulating the PM cavity effective length, i.e., either by adjusting the PM size or the effective refractive index, or by adjusting the y -direction fiber-PM centers displacement.

By defining the angular wavelength dispersion (AWD) for the two prongs, as⁵¹

$$\text{AWD} = \frac{\lambda_2 - \lambda_1}{\alpha_2 - \alpha_1} \quad (2)$$

where λ_2 and λ_1 are the wavelengths in which we detect the maximum power at the angular positions α_2 and α_1 respectively, we can observe that the transmission spectra corresponding to prong “1” (Figure 4a,b) and prong “2” (Figure 4c,d) demonstrate a 1.4 nm/° red shift and a −1.4 to 2.9 nm/° blue shift correspondingly. Figure 4e depicts the detected resonance wavelength as a function of the angular position α around the square and circular structures. If the SPP signal launching on the smooth film was to couple to waveguides, the coupling resonance wavelength could be fine-tuned by carefully selecting the angular position of the waveguide.

The structure operating wavelength range can be tuned across the whole spectrum range, from ultraviolet to infrared, by adjusting the period of the holes.¹⁵ If the structures were designed to work in the visible spectrum, they could also be useful for structural color applications. Spectrally pure and bright colors have been recently observed in transmission through periodically perforated plasmonic metasurfaces.⁵² In this case, the pixel size is restricted by the minimum number (~441) of holes required to observe the resonant transmission.⁴⁴ However, by selecting to observe the structural color through scattering on a defect located on the smooth film surrounding the PMs, the minimum pixel size limit is lifted enabling further reduction of the pixel size. Furthermore, exploiting the angular wavelength dispersion of the SPP beams launching from the PM, the structural color tone can be fine-tuned by purposely selecting the pixel angular position α around the PM. The use of the circular structure can render an even higher spectral purity, compared to the square structure, due to its narrower 3-dB bandwidth.

The inherent SPP angular wavelength dispersion is further enhanced by the substrate cavity reflections. The SPP transmission spectra at the prong angular positions before eliminating the substrate cavity have been plotted in Figure 4(f,g), by taking vertical cross sections of the Figure 3(b,e). To avoid any inconsistent power fluctuations, due to local sample impurities or faulty camera pixels, the power at a given angular position α was calculated by averaging the power over two adjacent 0.7° angular sections. The value of the AWD has been boosted to ± 0.03 nm/°, while the crosstalk, i.e., the unwanted coupling between the signal paths, has been decreased. By comparing the SPP power at two judiciously selected angular positions, small differences in wavelength values can be detected, making the PM structures suitable candidates for differential, microscale, high resolution wavemeters. In particular a 0.1 nm wavelength difference corresponds to a 12% power difference between two detectors (of 0.14° arc) positioned at the angular positions $\alpha = 84.9^\circ \pm 0.35^\circ$ and $\alpha = 88.4^\circ \pm 0.35^\circ$ around the square structure (Figure 4f), while a 0.06 nm wavelength difference corresponds to a 6% power difference between two detectors (of a 0.14° arc) positioned at the angular positions $\alpha = 91.2^\circ \pm 0.35^\circ$ and $\alpha = 91.3^\circ \pm 0.35^\circ$ circular structure. Through measuring small wavelength differences, the PM structures can also be used to sense small refractive index differences with potential applications in manufacturing quality control and diagnostics medicine.

To quantitatively investigate the effect of the PM boundary shape on the prong angular separation and power ratio, the SPP power angular distributions at the upper hemisphere of

the scattering ring surrounding the circular and square structures at the SPP forking spectral area ($\lambda = 1313$ nm/1319 nm), after eliminating the f-s and substrate cavities, have been plotted in Figure 5a, by taking horizontal cross sections of Figure 3(c,f). The prong angular separation, defined as the arc between the points that the output prong SPP beams impinge the scattering ring, for the circular structure (7.7°) is almost twice that for the square structure (4.2°). We have chosen to express the prong separation in degrees, so that its magnitude is independent of the radius of the scattering ring. The spatial distance of the two prongs expressed in μm increases proportionally with the distance from the illumination beam center.

Because of the large refractive index difference between air-nanostructured area interface and the air-Au smooth film interface, the SPP prongs refract at a direction almost perpendicular to the PM boundary, as schematically shown in Figure 5c (in which the illuminating beams are marked with red circles and the PM structures with gold outlines surrounding subwavelength holes assemblies). In the case of the square structure the output prong SPP beams propagate in almost parallel directions with the same polarization and maintaining the polarization of the illuminating light beam. In the case of the circular structure, the polarization for both the output prong SPP beams is linear with an azimuthal angle difference equal to the angle β between the points of refraction (7.7°). For a vertical (or horizontal) linear polarization, the polarization of each of the output SPP prongs will have a small azimuthal angle difference to the incident beam polarization; the sum of the azimuth angles differences between the polarization of each of the output SPP prongs and the illuminating beam is $\beta = 7.7^\circ$.

The power ratio of the prongs depend on the losses that they experience before detected and the number of scatterers contributing to their excitation.^{11,38} For symmetrical structures, like the ones under investigation, if the center of the illuminating beam coincided with the center of the crystal, the two prongs will have the same intensity,³⁸ demonstrating an 1 × 2/1 × 4 equal power (1:1/1:1:1:1) beam splitting functionality. However, if a horizontal x -misalignment between the PM center and the illuminating beam center is introduced, this symmetry breaks as schematically shown in Figure 5c. In the case of the circular structure, prongs “2” and “1” travel the same distance at the higher loss air-Au smooth film interface, while prong “2” travels a bit smaller distance at the lower loss air-nanostructured area interface experiencing a slightly lower loss, compared to prong “1”. However, this loss difference is largely outweighed from the fact that the number of scatterers contributing to prong “1” excitation is bigger than of those contributing to prong “2” excitation. Thus, prong “1” power is significantly higher (19.6%) than that of prong “2” allowing the structure to provide a 5:4/5:4:5:4 prong power ratio. Although the absolute detected power values of the prongs depend on the scattering ring radius, due to the SPP propagating losses at the air-gold interface, the prong power ratio is independent of the scattering ring radius.

By manipulating the x -displacement between the PM and the illuminating beam centers, the prong power ratio can be adjusted. For an equal magnitude x -displacement of the illuminating beam center in the opposite direction (+ direction) in respect to the PM center, prong “1” power would be lower than prong “2” power by the same percentage. The power difference between the circular structure prongs

could be used to monitor the magnitude and direction of the x -displacement between the PM and the illuminating beam centers, enabling the circular structure to be used as a high precision vectorial displacement sensor.

On the other hand, for the same PM-illuminating beam centers misalignment, the power difference between the prongs of the square structure is only 0.5%. Prong “1” experiences slightly higher losses traveling a slightly longer distance on the smooth air-Au interface before detection, while the number of scatterers contributing to the excitation of the prongs is the same. This allows the square structure to offer a robust $1 \times 2/1 \times 4$ equal power (1:1/1:1:1) splitting¹¹ which is practically insensitive (less than 1% power difference) to misalignment. Illuminating the square or the circular structures with a light beam polarized either circularly or linearly at $\pm 45^\circ$, instead of vertically or horizontally polarized, would allow the simultaneous excitation of the $(0, \pm 1)_a$ and the $(\pm 1, 0)_a$ eigenmodes¹⁰ and consequently render a 1×8 , instead of 1×4 , beam-splitting, as well as enable the simultaneous x - and y -axes vectorial displacement sensing, when the circular structure is used.

To investigate the effect of the reflections happening in the f -s and the substrate cavities on the SPP beam splitting, the corresponding SPP power angular profiles at the upper hemisphere of the scattering ring surrounding the square and circular structures as detected (i.e., before eliminating the f -s and substrate cavities) and after eliminating only the f -s cavity, but not the substrate cavity, have been plotted in Figure 5b, by taking horizontal cross sections of Figure 3(a,b,d,e). The power difference between the circular structure prongs “1” and “2” is reduced to 9.5% when neither of the cavities is eliminated and to only 0.8% if only the f -s is eliminated. In the case of the square structure, $\lambda = 1319$ nm, the SPP power splitting has been canceled by the substrate cavity interferences; this is the reason the SPP power splitting is not visible at the square structure far-field image (Figure 2b).

CONCLUSIONS AND OUTLOOK

In summary, we have experimentally demonstrated multifunctional, planar structures based on periodically perforated plasmonic metasurfaces operating at telecom wavelengths and integrating several key functionalities, namely light-to-surface plasmon coupling, 1×4 (or 1×8) controllable beam-splitting, wavelength filtering and routing, high resolution differential wavelength measurement, and vectorial displacement sensing—all in a single microscale structure. The beam splitting functionality is based on the zero group velocity that the eigenmodes experience as they flatten to avoid crossing at the vicinity of the SPP bandgap spectral regions. In contrast to the beam splitters based on the partial reflection of a plasmonic beam^{23,24,28,29} where the output SPP prongs propagate orthogonally with orthogonal polarizations, the output prongs of our structures propagate in either (anti)parallel directions or forming small angles between them, with similar polarizations to each other and retaining to a relatively high degree the polarization of the incident light beam. Furthermore, they launch on the smooth metal film surrounding the plasmonic metasurfaces without blocking the transmission of the input light beam through the nanostructured area, thereby allowing for nondestructive sampling or sensing and parallel processing of the beam. Operating several beam splitters in parallel could lead to higher generation rates in a quantum random number

generator²⁸ or increase the processing power and speed of an integrated photonic or quantum processor.

By characterizing plasmonic metasurface structures with the same lattice parameters but different boundary shapes, viz. circular and square, we have shown that the structure functionality parameters, such as sensitivity to misalignment, prong angular separation, power ratio controllability, polarization and bandwidth, can all be adjusted by designing the boundary shape of the plasmonic metasurfaces. We have found that a square structure offers a robust, insensitive to misalignment, equal power beam splitting, while in a circular structure the prong power ratio can be controlled by adjusting the displacement between the light illuminating beam and the plasmonic metasurface nanostructure centers. The illuminating beam-plasmonic nanostructure alignment can be manipulated passively, by design, or actively, using for instance piezoelectric systems, thereby reducing the need for custom-made predetermined designs and enabling the realization of microscale integrated circuits with adaptable functionality. Moreover, the circular structure could operate as a differential vectorial displacement sensor, capable of monitoring simultaneously the magnitude and the direction of the displacement between the illuminating beam and the plasmonic metasurface centers by comparing the output prong power values. While the SPP signal power in our experiment is measured off-plane after converting to photons, one could envision the integration of the plasmonic metasurfaces with in-plane detectors,⁵³ enabling a completely standalone device.

In addition to the above, both classes of structures operate as bandpass filters; the square structure 3-dB bandwidth (53 nm) is almost double than that of the circular structure (35 nm). Each of the prongs experience an angular wavelength dispersion, leading the resonance wavelength to red-shift or blue-shift depending on the direction of the propagation. If the output prong SPP beams were to couple in waveguides, the coupling wavelength could be fine-tuned by carefully selecting the width and the angular position of the waveguide. Although the structures were designed to operate in the O-band telecom wavelength range, the operating wavelength can be tuned across the whole range, from ultraviolet to infrared by changing the plasmonic metasurface lattice period.¹⁵ If the structures were designed to operate in the visible spectrum, they could also be useful for structural color applications.⁵² By choosing to observe the structural color in the surrounding smooth metal film through scattering on a defect, rather than in transmission through the nanostructured area,⁵² a smaller pixel size can be achieved. Moreover, exploiting the angular wavelength dispersion of the prongs, the color tone can be fine-tuned by judiciously selecting the angular position of the pixels. Using a circular structure, a higher spectral purity could be achieved due to its narrower bandwidth, as compared to a square structure.

We note in closing that the reflections and interferences happening in the substrate Fabry–Perot cavity highly enhance the prong angular wavelength dispersion, while decreasing the crosstalk. This allows the PM structures to operate as high-resolution, planar, microscale, differential wavemeters. For instance, a 0.1 nm wavelength difference corresponds to a 12% power difference between two angular positions around the square structure, while a 0.06 nm wavelength difference corresponds to a 6% power difference between two angular positions around the square structure. High-resolution microscale wavemeters could also be used to measure small

differences in refractive indices, with potential useful applications in diagnostics medicine and manufacturing quality control sectors.

The compact, easily controllable, and all-in-one nature of the plasmonic metasurface structures presented in this work makes them suitable for a variety of applications, ranging from tight integration in on-chip devices to medical diagnostics, phototherapy, manufacturing quality control, space missions, and optical or quantum computing and short-range communication systems.

AUTHOR INFORMATION

Corresponding Author

Maria I. Benetou – *Mbh-Qet. Ltd., London EC1V 2NX, United Kingdom*; orcid.org/0000-0001-5655-393X;
Email: mbenetou@mbhqet.com

Author

Kosmas L. Tsakmakidis – *Section of Condensed Matter Physics, Department of Physics, National and Kapodistrian University of Athens, GR-15784 Athens, Greece*

Complete contact information is available at:

<https://pubs.acs.org/10.1021/acsp Photonics.0c01530>

Notes

The authors declare no competing financial interest.

ACKNOWLEDGMENTS

We would like to thank the Photonics and Nanotechnology group, Department of Physics, King's College London, UK, for providing the samples and SEM images, as well as the Optical Networks Group, Department of Electronic & Electrical Engineering, University College London, UK, for therein performing the reported measurements as part of M.I.B.'s PhD research. M.I.B. acknowledges EPSRC, UK, for a PhD scholarship funding. K.L.T. was supported by the General Secretariat for Research and Technology (GSRT) and the Hellenic Foundation for Research and Innovation (HFRI), Greece, under Grant No. 1819. The authors also wish to thank Nicolae C. Panou for feedback during the preparation of the manuscript.

REFERENCES

- (1) Haffner, C.; et al. All-plasmonic Mach–Zehnder modulator enabling optical high-speed communication at the microscale. *Nat. Photonics* **2015**, *9*, 525.
- (2) Maier, S. A.; Brongersma, M. L.; Kik, P. G.; Meltzer, S.; Requicha, A. A. G.; Atwater, H. A. Plasmonics—A Route to Nanoscale Optical Devices. *Adv. Mater.* **2001**, *13* (19), 1501–1505.
- (3) Gramotnev, D. K.; Bozhevolnyi, S. I. Plasmonics beyond the diffraction limit. *Nat. Photonics* **2010**, *4*, 83.
- (4) Haffner, C.; et al. Low-loss plasmon-assisted electro-optic modulator. *Nature* **2018**, *556* (7702), 483–486.
- (5) Bogdanov, S. I.; Boltasseva, A.; Shalaev, V. M. Overcoming quantum decoherence with plasmonics. *Science* **2019**, *364* (6440), 532.
- (6) Papaioannou, S.; Kalavrouziotis, D.; Vyrsoinos, K.; Weeber, J.-C.; Hassan, K.; Markey, L.; Dereux, A.; Kumar, A.; Bozhevolnyi, S. I.; Baus, M.; Tekin, T.; Apostolopoulos, D.; Avramopoulos, H.; Pleros, N. Active plasmonics in WDM traffic switching applications. *Sci. Rep.* **2012**, *2* (1), 652.
- (7) Pu, M.; Ma, X.; Li, X.; Guo, Y.; Luo, X. Merging plasmonics and metamaterials by two-dimensional subwavelength structures. *J. Mater. Chem. C* **2017**, *5* (18), 4361–4378.

- (8) Jiang, N.; Zhuo, X.; Wang, J. Active Plasmonics: Principles, Structures, and Applications. *Chem. Rev.* **2018**, *118* (6), 3054–3099.
- (9) Stockman, M. I.; et al. Roadmap on plasmonics. *J. Opt.* **2018**, *20* (4), 043001.
- (10) Benetou, M.; Thomsen, B.; Bayvel, P.; Dickson, W.; Zayats, A. Four-level polarization discriminator based on a surface plasmon polaritonic crystal. *Appl. Phys. Lett.* **2011**, *98* (11), 111109.
- (11) Benetou, M. I. SPPC Based Beam Splitter and Alignment Sensor: The Passive and Active Control of its Functionality Parameters. In *Frontiers in Optics + Laser Science APS/DLS*; Optical Society of America: Washington, DC, 2019; p JW3A.68.
- (12) Benetou, M. I. *Surface Plasmon Polaritonic Crystals for Applications in Optical Communications*; University College London: London, UK, 2019. <https://discovery.ucl.ac.uk/id/eprint/10083752/>.
- (13) Schuller, J. A.; Barnard, E. S.; Cai, W.; Jun, Y. C.; White, J. S.; Brongersma, M. L. Plasmonics for extreme light concentration and manipulation. *Nat. Mater.* **2010**, *9*, 193.
- (14) Brongersma, M. L.; Shalaev, V. M. The Case for Plasmonics. *Science* **2010**, *328* (5977), 440.
- (15) Genet, C.; Ebbesen, T. W. Light in tiny holes. *Nature* **2007**, *445*, 39.
- (16) Sorger, V. J.; Oulton, R. F.; Ma, R.-M.; Zhang, X. Toward integrated plasmonic circuits. *MRS Bull.* **2012**, *37* (8), 728–738.
- (17) Wu, X.; et al. On-Chip Single-Plasmon Nanocircuit Driven by a Self-Assembled Quantum Dot. *Nano Lett.* **2017**, *17* (7), 4291–4296.
- (18) Huang, K. C. Y.; Seo, M.-K.; Sarmiento, T.; Huo, Y.; Harris, J. S.; Brongersma, M. L. Electrically driven subwavelength optical nanocircuits. *Nat. Photonics* **2014**, *8* (3), 244–249.
- (19) Tame, M. S.; McEnery, K. R.; Özdemir, Ş. K.; Lee, J.; Maier, S. A.; Kim, M. S. Quantum plasmonics. *Nat. Phys.* **2013**, *9* (6), 329–340.
- (20) Holtfrerich, M. W.; Dowran, M.; Davidson, R.; Lawrie, B. J.; Pooser, R. C.; Marino, A. M. Toward quantum plasmonic networks. *Optica* **2016**, *3* (9), 985–988.
- (21) Zhu, T.; Zhou, Y.; Lou, Y.; Ye, H.; Qiu, M.; Ruan, Z.; Fan, S. Plasmonic computing of spatial differentiation. *Nat. Commun.* **2017**, *8* (1), 15391.
- (22) AbdollahRamezani, S.; Arik, K.; Khavasi, A.; Kavehvas, Z. Analog computing using graphene-based metalines. *Opt. Lett.* **2015**, *40* (22), 5239–5242.
- (23) Kasture, S. Designing optical circuits using plasmonic beam splitters. *Opt. Lett.* **2018**, *43* (11), 2547–2550.
- (24) Vest, B.; et al. Anti-coalescence of bosons on a lossy beam splitter. *Science* **2017**, *356* (6345), 1373.
- (25) Hou, J.; Slowik, K.; Lederer, F.; Rockstuhl, C. Dissipation-driven entanglement between qubits mediated by plasmonic nano-antennas. *Phys. Rev. B: Condens. Matter Mater. Phys.* **2014**, *89* (23), 235413.
- (26) Martín-Cano, D.; González-Tudela, A.; Martín-Moreno, L.; García-Vidal, F. J.; Tejedor, C.; Moreno, E. Dissipation-driven generation of two-qubit entanglement mediated by plasmonic waveguides. *Phys. Rev. B: Condens. Matter Mater. Phys.* **2011**, *84* (23), 235306.
- (27) Gonzalez-Tudela, A.; Martin-Cano, D.; Moreno, E.; Martin-Moreno, L.; Tejedor, C.; Garcia-Vidal, F. J. Entanglement of Two Qubits Mediated by One-Dimensional Plasmonic Waveguides. *Phys. Rev. Lett.* **2011**, *106* (2), 020501.
- (28) Francis, J. T.; Zhang, X.; Özdemir, Ş. K.; Tame, M. Quantum random number generation using an on-chip plasmonic beamsplitter. *Quantum Science and Technology* **2017**, *2* (3), 035004.
- (29) Di Martino, G.; et al. Observation of Quantum Interference in the Plasmonic Hong-Ou-Mandel Effect. *Phys. Rev. Appl.* **2014**, *1* (3), 034004.
- (30) Hong, C. K.; Ou, Z. Y.; Mandel, L. Measurement of subpicosecond time intervals between two photons by interference. *Phys. Rev. Lett.* **1987**, *59* (18), 2044–2046.
- (31) Gan, Q.; et al. Plasmonic surface-wave splitter. *Appl. Phys. Lett.* **2007**, *90* (16), 161130.

- (32) Fu, Z.; Gan, Q.; Gao, K.; Pan, Z.; Bartoli, F. J. Numerical Investigation of a Bidirectional Wave Coupler Based on Plasmonic Bragg Gratings in the Near Infrared Domain. *J. Lightwave Technol.* **2008**, *26* (22), 3699–3703.
- (33) López-Tejeda, F.; et al. Efficient unidirectional nanoslit couplers for surface plasmons. *Nat. Phys.* **2007**, *3* (5), 324–328.
- (34) Gan, Q.; Gao, Y.; Wagner, K.; Vezenov, D.; Ding, Y. J.; Bartoli, F. J. Experimental verification of the rainbow trapping effect in adiabatic plasmonic gratings. *Proc. Natl. Acad. Sci. U. S. A.* **2011**, *108* (13), 5169.
- (35) Barnes, W. L.; Preist, T. W.; Kitson, S. C.; Sambles, J. R. Physical origin of photonic energy gaps in the propagation of surface plasmons on gratings. *Phys. Rev. B: Condens. Matter Mater. Phys.* **1996**, *54* (9), 6227–6244.
- (36) Tsakmakidis, K. L.; Hess, O.; Boyd, R. W.; Zhang, X. Ultraslow waves on the nanoscale. *Science* **2017**, *358* (6361), eaan5196.
- (37) Altwischer, E.; Ma, X.; Exter, M. P. v.; Woerdman, J. P. Resonant Bragg scatter of surface plasmons on nanohole arrays. *New J. Phys.* **2006**, *8* (4), 57–57.
- (38) Benetou, M. I.; Bouillard, J.-S.; Segovia, P.; Dickson, W.; Thomsen, B. C.; Bayvel, P.; Zayats, A. V. Boundary effects in finite size plasmonic crystals: focusing and routing of plasmonic beams for optical communications. *Nanotechnology* **2015**, *26* (44), 444001.
- (39) Sandtke, M.; Kuipers, L. Slow guided surface plasmons at telecom frequencies. *Nat. Photonics* **2007**, *1* (10), 573–576.
- (40) DeBra, D. B. Drag-free control for fundamental physics missions. *Adv. Space Res.* **2003**, *32* (7), 1221–1226.
- (41) Tao, S.; Dong, X.; Lai, B. Temperature-insensitive fiber Bragg grating displacement sensor based on a thin-wall ring. *Opt. Commun.* **2016**, *372*, 44–48.
- (42) Zoellner, A.; et al. Differential optical shadow sensor for sub-nanometer displacement measurement and its application to drag-free satellites. *Opt. Express* **2017**, *25* (21), 25201–25211.
- (43) Bao, W.; Rong, Q.; Chen, F.; Qiao, X. All-fiber 3D vector displacement (bending) sensor based on an eccentric FBG. *Opt. Express* **2018**, *26* (7), 8619–8627.
- (44) Garcia-Vidal, F. J.; Martin-Moreno, L.; Ebbesen, T. W.; Kuipers, L. Light passing through subwavelength apertures. *Rev. Mod. Phys.* **2010**, *82* (1), 729–787.
- (45) Ghaemi, H. F.; Thio, T.; Grupp, D. E.; Ebbesen, T. W.; Lezec, H. J. Surface plasmons enhance optical transmission through subwavelength holes. *Phys. Rev. B: Condens. Matter Mater. Phys.* **1998**, *58* (11), 6779–6782.
- (46) Zayats, A. V.; Smolyaninov, I. I.; Maradudin, A. A. Nano-optics of surface plasmon polaritons. *Phys. Rep.* **2005**, *408* (3–4), 131–314.
- (47) Billaudeau, C.; Collin, S.; Sauvan, C.; Bardou, N.; Pardo, F.; Pelouard, J.-L. Angle-resolved transmission measurements through anisotropic two-dimensional plasmonic crystals. *Opt. Lett.* **2008**, *33* (2), 165–167.
- (48) Salomon, L.; Grillot, F.; Zayats, A. V.; de Fornel, F. Near-field distribution of optical transmission of periodic subwavelength holes in a metal film. *Phys. Rev. Lett.* **2001**, *86* (6), 1110–1113.
- (49) Zayats, A. V.; Smolyaninov, I. I. Near-field photonics: surface plasmon polaritons and localized surface plasmons. *J. Opt. A: Pure Appl. Opt.* **2003**, *5* (4), S16.
- (50) Gao, H.; Zhou, W.; Odom, T. W. Plasmonic Crystals: A Platform to Catalog Resonances from Ultraviolet to Near-Infrared Wavelengths in a Plasmonic Library. *Adv. Funct. Mater.* **2010**, *20* (4), 529–539.
- (51) Benetou, M. I.; Dickson, W.; Mikhailov, V.; Thomsen, B.; Bayvel, P.; Zayats, A. V. Dispersive Properties of Surface Plasmon Polaritonic Crystals with Different Boundary Shapes. In *IEEE LEOS Annual Meeting Conference Proceedings*, Antalya, Turkey, 2009; pp 100–101.
- (52) Kristensen, A.; Yang, J. K. W.; Bozhevolnyi, S. I.; Link, S.; Nordlander, P.; Halas, N. J.; Mortensen, N. A. Plasmonic colour generation. *Nature Reviews Materials* **2017**, *2*, 16088.
- (53) Berini, P. Surface plasmon photodetectors and their applications. *Laser & Photonics Reviews* **2014**, *8* (2), 197–220.